nature communications

Article

https://doi.org/10.1038/s41467-026-75619-z

Orthogonal assembly of hetero-porous structures by reversible adaptation for efficient isomeric separation

Received: 6 November 2025

Accepted: 7 July 2026

Published online: 15 July 2026

Check for updates

Qi Mou[1,5], Changpin Chen[1,5], Xin Li[1,5], Tianyi Zheng[2], Jiahao Wang[1], Yaxin Shang[1], Yongri Liang[3] ✉, Hulin Tai[4], Long Yi Jin[4], Yi Zhang[1], Zhegang Huang[1] ✉ & Myongsoo Lee[2] ✉

Isomers separation is a challenging but crucial process in biological and chemical processes. Mixed-matrix membranes (MMMs) combining selective adsorbents within the polymer matrix have the potential for separating isomeric mixtures. However, the limited compatibility is a significant problem for efficient separation with appropriate permeability and selectivity. Herein, we report the rational design and construction of a highly oriented multi-porous membrane by the orthogonal assembly of hydrogen-bonded macrocycle amphiphiles through dynamic adaptation. The macrocycles can undergo helical propagation in the vertical direction with hydrophilic exteriors, forming lyotropic liquid crystal gels. By simultaneous control of immiscible pores with identical hydrogen bonding, well-aligned chiral nanochannels are created in gel matrix, enabling precise molecular sieving with separation factor of 11.46 for constitutional isomer and 92% ee for enantiomer. The strategy follows the principle of dynamic chemistry, providing a versatile platform for energy-efficient separations in chiral resolution, fine chemical purification and biomimetic transport systems.

The efficient separation of isomeric molecules is essential in various chemical and biological processes, but it remains a significant challenge due to their similar physicochemical properties, such as molecular size, shape, and functional group distribution[1,2]. In biological systems, molecular transport across membranes is highly efficient and selective, facilitated by specific proteins that exhibit regioselectivity and stereoselectivity[3,4]. The natural selectivity has inspired significant efforts in developing synthetic membranes capable of mimicking these properties[5,6]. Among various approaches, mixed-matrix membranes (MMMs), which incorporate permeable fillers with selective adsorption into polymer matrices, have shown great potential for efficient molecular separation[7,8]. For example, metal-organic frameworks (MOFs)[9,10], covalent organic frameworks (COFs)[11,12], porous organic cages (POCs)[13], and zeolites[14] have been successfully used as isotropic or anisotropic fillers into polymer networks to improve the selectivity as well as the permeability. Particularly, the fillers with anisotropic structures offer substantial advantages over isotropic fillers[15]. The relatively large external surface area permits high filler loading, and the combination of short diffusion pathways with preferential molecular transport can significantly increase both permeability and selectivity[16,17]. However, the ideal performance cannot be persistent in the elaborated polymer membranes because of inevitable phase separation from immiscible blocks[18,19].

[1]PCFM, GTRCSSTC and GD HPPC Lab, School of Chemistry Sun Yat-sen University, Guangzhou, China. [2]Department of Chemistry, Fudan University, Shanghai, China. [3]State Key Lab of Metastable Materials Science and Technology, School of Materials Science and Engineering, Yanshan University, Qinhuangdao, China. [4]National Demonstration Centre for Experimental Chemistry Education, Department of Chemistry, Yanbian University, Yan Bian Chao Xian Zu Zi Zhi Zhou, Yanji, China. [5]These authors contributed equally: Qi Mou, Changpin Chen, Xin Li. ✉e-mail: liangyr@ysu.edu.cn; huangzhg3@mail.sysu.edu.cn; mslee@fudan.edu.cn

Orthogonal assembly of hetero-porous precursors driven by noncovalent interactions represents an alternative to solve this problem[20,21]. Hybrid structures with different pore sizes or shapes can be well tailored into a thin membrane. However, the efficient sieving is still limited due to the blocking of selectively adsorbing pores[22]. The key reason is that it is hard to simultaneously control the formation of two kinds of pores bearing different affinities, in which various driving forces are used in the assembly of heterogeneous structures[23]. Unfortunately, the strong driving forces inhibit the weak ones, preventing their widespread application. To address this challenge, self-repairing can be envisioned for generating polymeric networks with an ordered internal porous structure[24,25]. Hydrogen-bonded macrocycles (HBMs), as a class of developing porous precursors, are highly versatile towards unidirectional interaction[26]. For example, much of the hydrogen host–guest interaction at the periphery of flat macrocycles would cause multiple noncovalent interactions to produce stable two-dimensional scaffolds with regular pore sizes and shapes[27]. Whereas, the noncovalent interaction surrounding macrocycle skeletons exhibits special recognition for hydrogen donor and acceptor motifs, which can be formed, broken, and reformed, leading to the formation of the most stable thermodynamical structures through a self-checking process[28]. In view of above advantages, here, the amphiphilic hydrogen-bonded aromatic macrocycles (HBAMs) that form highly organized anisotropic MMMs through orthogonal assembly were presented by host–guest interaction of bent-shaped aromatic amphiphiles containing phenol and phenolate at both edges of the aromatic segment for intermolecular hydrogen bonding, which was decorated by a hydrophilic oligoether dendron at its apex (Fig. 1). The noncovalent HBAMs would autonomously propagate into one-dimensional helical fillers with amphiphilic exteriors, which are great suited for subsequent generation of gel matrix. Importantly, the skeletons based on dynamic hydrogen bonds were obviously flexible

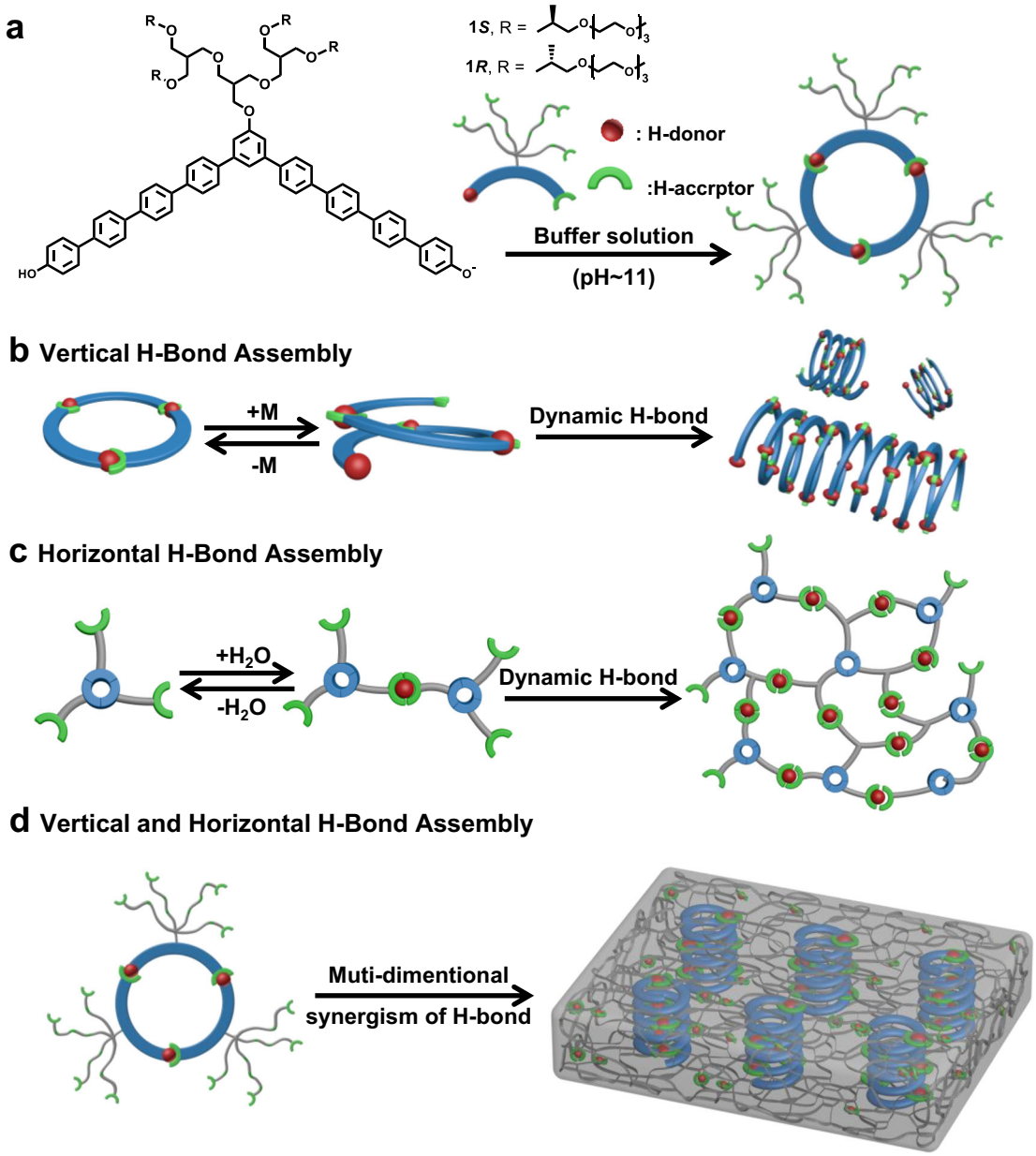

Fig. 1 | Shape persistent mixed-matrix membranes with the multiple embedding of chiral fillers. a The bent-shaped aromatic amphiphiles ***1S***, ***1R*** form HBAMs in buffer solution (pH-11) through hydrogen-bonded host–guest recognition. **b**, **c** The formation of 1D helices (**b**) and polymer networks (**c**) from single vertical or horizontal dynamic H-bond assembly. **d** Schematic representation of the strategy for the construction of anisotropic HOG membrane with multiple helical fillers through synergistic dynamic H-bond.

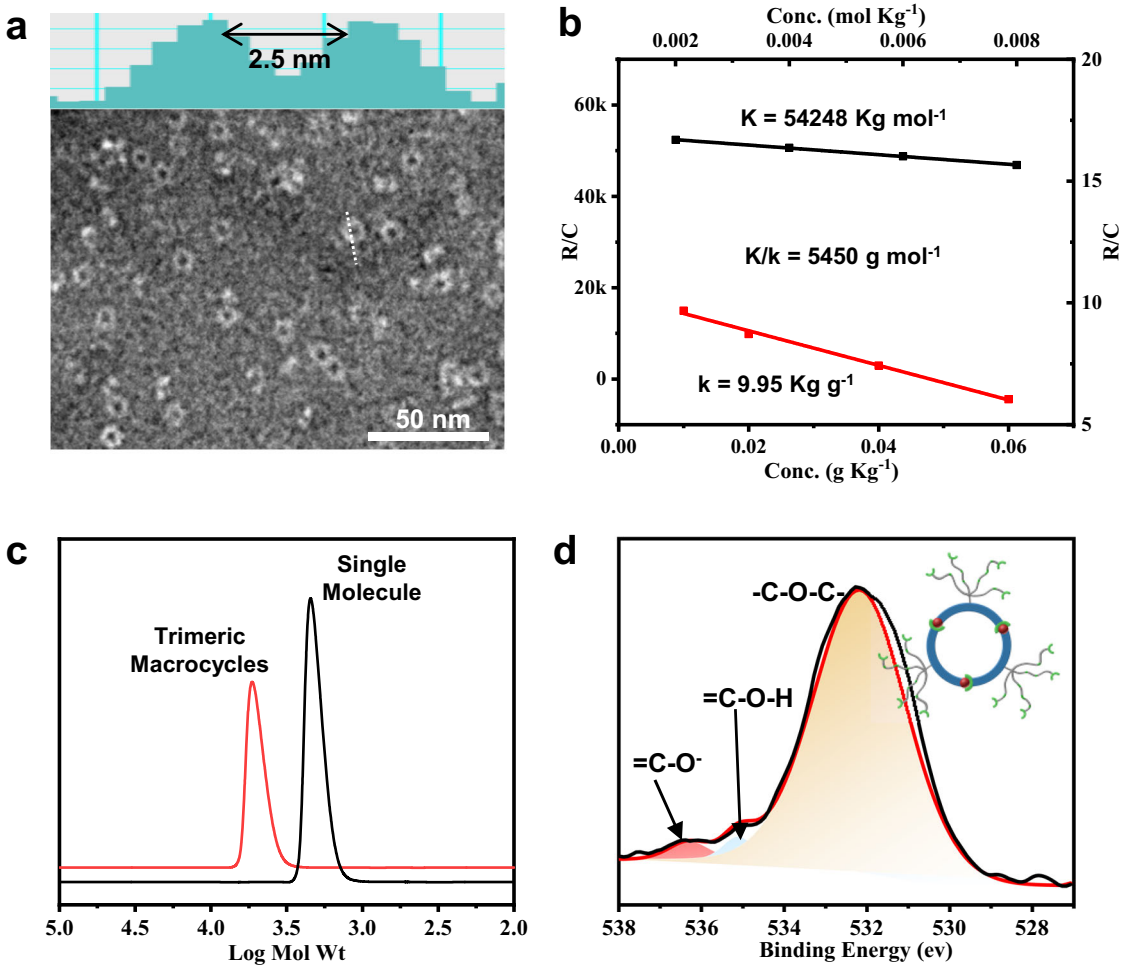

Fig. 2 | Trimeric macrocycles from host–guest recognition. a TEM image of toroidal aggregates from the buffer solution of **1*S*** (11 μM, Na_2HPO_4/NaOH). **b**, **c** The weights of trimeric **1*S*** from VPO (**b**) and GPC results (**c**). **d** XPS spectra of *O1s* from freeze-drying of **1*S*** in buffer solution (11 μM, Na_2HPO_4/NaOH).

under gelation, allowing a self-repairing process along the filler axis to generate highly ordered lyotropic liquid crystal gels. The optimization of helical fillers in gel matrix based on thermodynamical control could create well-defined paths to enhance both regioselectivity and enantioselectivity in selective molecular transport. The comprehensive behavior highlighted in this work represents a strategy for energy-efficient membrane separation to open the door in a range of sieving fields from fine chemical purification to biomimetic systems.

Results

Designed noncovalent macrocycles and helical propagation

Owing to the neutralization of both hydroxyl segments, the molecules exhibited solubility in sodium hydroxide solution. However, the addition of phosphoric acid to a buffer solution until the pH reaches 11 drove the molecules of **1*S*** (11 μM) with tetra-phenylene branches to aggregate into toroidal objects (Fig. 2a). Atomic force microscopy (AFM) revealed uniform toroids with a height of 0.4 nm, indicating that these toroidal objects were unilaminar macrocycles (Supplementary Fig. 3a). The weight of the toroid based on the primary aggregation of **1*S*** was measured as 5450 g mol^{-1} by Vapor Pressure Osmometry (VPO) in triethylamine in the concentration range of 0.01–0.06 g kg^{-1} (Fig. 2b and Supplementary Fig. 3b). The aggregation weight was further analyzed by gel permeation chromatography (GPC) using the buffer solution (Na_2HPO_4/NaOH, pH-11) as the eluant to be 1.04 times as less as VPO result, which was three times as large as single molecule (Fig. 2c). To gain insight into the formation of primary trimeric macrocycles, X-ray photoelectron spectroscopy (XPS) experiments were conducted. In the high-resolution spectra, two binding energies of *O1s* were observed at 535.8 eV (=C–O–) and 531.3 eV (C–O–C) (Supplementary Fig. 3d), indicating the formation of phenolates at both edges of the aromatic segment in a strongly alkaline solution[29,30]. However, upon the addition of phosphoric acid up to a buffer solution (Na_2HPO_4/NaOH), the peak of phenolate was significantly reduced, and a new peak of phenol with a low binding energy appeared (Fig. 2d)[31]. The ratio of the peak areas between phenol and phenolate was close to one, indicating that one aromatic edge of **1*S*** was protonated from phenolate into phenol, resulting in intermolecular hydrogen bonding with neighboring molecules at both ends of the aromatic segment, which, in turn, folded each other into closed trimeric macrocycles.

Importantly, the molecular weights gradually increased from 8072 to 14765 as the concentration increased from 0.07 to 0.3 g kg^{-1} (Supplementary Fig. 5a), suggesting that the closed noncovalent macrocycles may undergo a transition between eclipsed helix and slipped larger macrocycles by the insertion of additional molecules[32]. To corroborate the subsequent structures, we performed optical experiments with the variation of concentration. As the concentration increased, the absorption maximum of **1*S*** gradually blue-shifted with respect to the trimeric macrocycles (Supplementary Fig. 4a), indicating that the elongated chromophores adopted an eclipsing conformation. The dramatic increase of the cotton effect from circular dichroism (CD) revealed that the eclipsing occurs in a preferred coil direction (pH 11, 11–550 μM, Fig. 3a), leading to chiral transfer from the asymmetric dendritic segment into rigid chromophores[33]. The fiction

https://doi.org/10.1038/s41467-026-75619-z

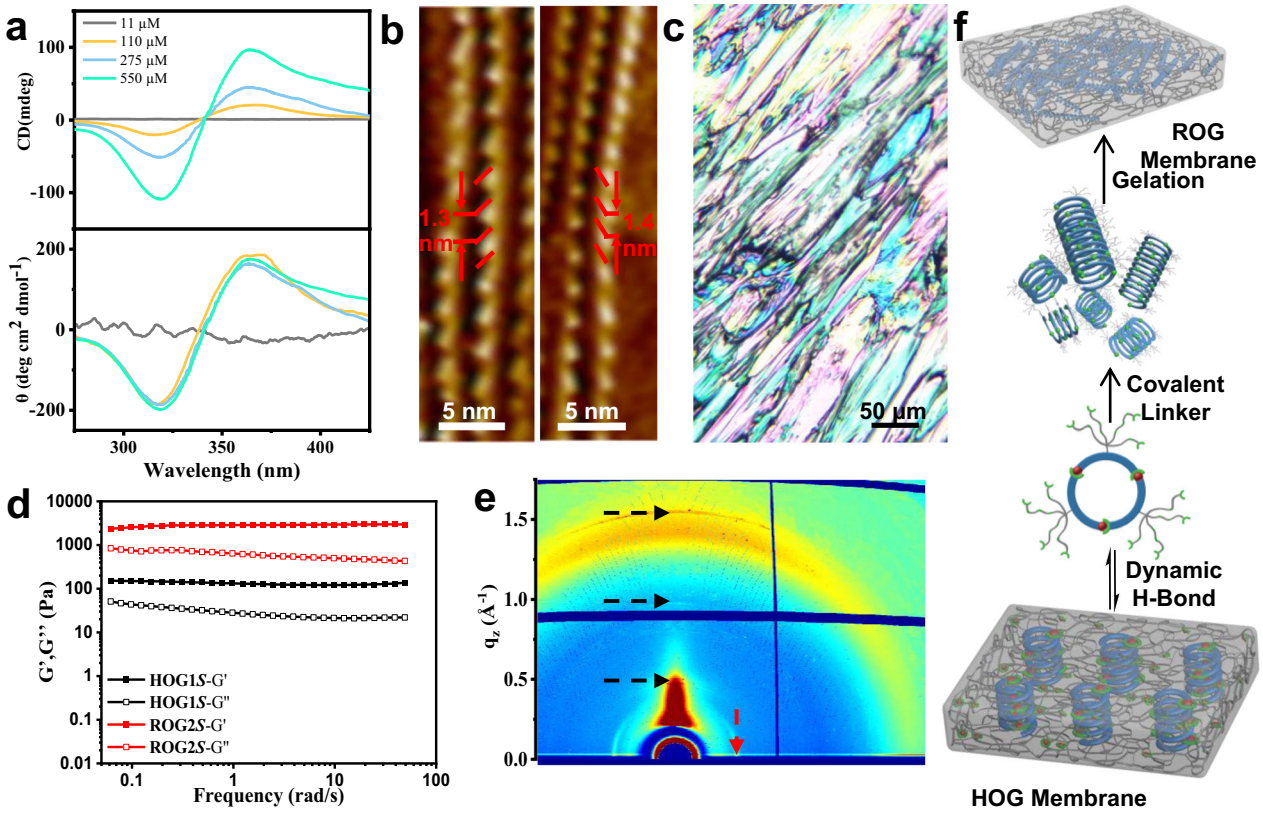

Fig. 3 | Helical propagation and its alignment in the formation of an anisotropic gel. a CD-spectra of **1*S*** in buffer solution (Na_2HPO_4/NaOH) with the variation of concentration. **b** AFM phase images of right-handed **1*S*** (left) and left-handed **1*R*** (right) from the evaporation of buffer solution (110 μM, Na_2HPO_4/NaOH). **c** Polarized optical micrograph of lyotropic liquid crystal gel of **1*S*** in buffer solution (Na_2HPO_4/NaOH). **d** G′ and G″ values of highly ordered HOGs of **1*S*** (22 mM, buffer solution: Na_2HPO_4/NaOH) and amorphous ROGs of **2*S*** (4 wt%, aqueous solution) on frequency sweep (from 0.01 to 100 rad s^{-1}). **e** 2D-GIWAXS pattern of **1*S*** from the evaporation of buffer solution (110 μM, Na_2HPO_4/NaOH), black arrow: out-of-plane direction, red arrow: in-plane direction. **f** Schematic representation for the formation of ROG membrane by random orientation of helical fillers and anisotropic HOG membrane with multiple alignment of helical fillers.

of molecular chirality is also illustrated by a mirror-image relationship with the opposite enantiomer **1*R*** (Supplementary Fig. 5b). Transmission electron microscopy (TEM) from the evaporation of dense buffer solution (110 μM) showed elongated cylindrical objects with regular diameter of 7 nm, whereas initial toroid with identical outside diameter could be observed occasionally in the images (Supplementary Fig. 6a). These results demonstrated that the insertion of additional molecules trigger the original trimeric macrocycles to be active, enabling them to coil with each other with mutual rotation in the same direction to form elongated helical tubes in buffer solution (Fig. 3b).

Spontaneous gelation of helical coils

Owing to the periodical location of oligoether dendrimers at the exterior of the elongated helix, the dilute solution undergoes spontaneous gelation at concentrations above 22 mM, and the resulting gels appear to be strongly birefringent (Fig. 3c and Supplementary Fig. 5d). The dynamic viscoelasticity of **1*S*** in Na_2HPO_4/NaOH buffer solutions (22 mM) shows frequency-independent storage modules (G′), which are much larger than the loss modulus (G″) (Fig. 3d). These results indicated the formation of gel-like lyotropic liquid crystals. To elucidate the ordered structures, small- and wide-angle X-ray experiments were performed on freeze-dried **1*S***. The small-angle X-ray scattering of **1*S*** showed four sharp reflections (Supplementary Fig. 6e), which can be indexed to a 2D tetragonal structure with a lattice constant of 3.5 nm. In addition, three low reflections appeared with a spacing ratio of 1:2:3, suggesting the existence of periodicity in the direction of the stacks of repeating units. (Supplementary Fig. 6f). To clarify the ordered structures, the X-ray beam was impinged on the film surface, and the 2D grazing incidence wide-angle scattering (GIWAXS) was further performed with an incidence angle α_i of 0.2°. The GIWAXS of **1*S*** displayed an isotropic scattering ring at around 1.4 $Å^{-1}$ and intense scattering arcs at around 0.5 $Å^{-1}$, 1.0 $Å^{-1}$, and 1.5 $Å^{-1}$ with equidistant q-spacing along the out-of-plane direction (Fig. 3e). The isotropic scattering ring is assignable to an amorphous interaction of ethylene oxide segments[34], and the scattering arcs originate from an ordered structure. The calculated equal distance (1.3 nm) was attributable to the pitch of helical tubules, which was well matched with the results of the AFM experiments. On the other hand, an obvious scattering arc appeared at around 0.36 $Å^{-1}$ along the in-plane direction in the 2D GIWAXS pattern, indicative of the formation of additional ordering perpendicular to the helical column axis. Considering the direction of the tubular axis in out-of-plane, the d-spacing (3.5 nm) from in-plane scattering is regarded as the tubular radius. On the basis of these results, the number of repeating units per pitch can be calculated according to the density measurements[35]. The calculation shows that the pitch of a single helix is composed of sixteen repeating units, giving rise to a coiled helical column with a 2.5 nm hydrophobic pore.

The multiple organization of helical columns can be explained by a dynamic H-bonding behavior of the helical backbone in the formation of highly ordered gels (**HOG1*S***). When the amphiphilic columns dissolve into aqueous solution, ethylene oxide chains are fully hydrated and wrap up hydrophobic helical segments to become a random helix with different lengths (10 nm–3 μm) (Supplementary Fig. 6a, c). During gelation, however, the ethylene oxide chains would be dehydrated and collapse into globules, which minimizes the effective hydrophilic volume due to the loss of the hydrogen bonding between

https://doi.org/10.1038/s41467-026-75619-z

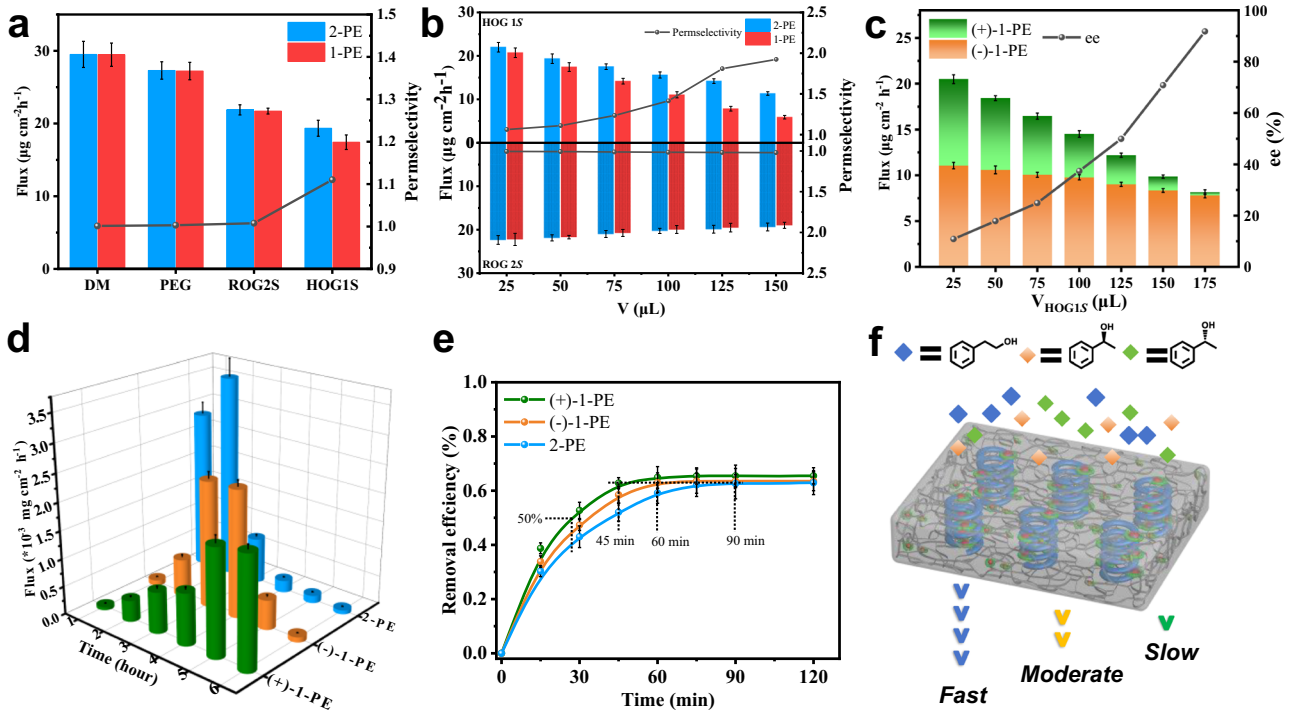

Fig. 4 | Comprehensive separation performance of HOG membranes for phenylethanol isomers. a Fluxes and permselectivity of 2-PE and 1-PE in aqueous solution (0.02 wt%) with a series of membranes. **b** Fluxes and permselectivity of 2-PE and 1-PE in aqueous solution (0.02 wt%) with the loading of **ROG2*S*** and **HOG1*S***. **c** Fluxes and enantiomeric excess of racemic mixture of (±)−1-PE aqueous solution (0.01 wt%) with the variation of **HOG1*S*** loading. **d** Cascade separation of an equally mixed solution of 2-PE, (-)−1-PE and (+)−1-PE (0.01 wt%) by the use of **HOG1*S*** membrane. **a**–**d** The error bars on the *y* axis represent the standard deviation of the fluxes measured in the membrane separation tests ($n = 3$, see details in "Methods"). **e** Kinetic removal abilities of **HOG1*S*** for 2-PE, (-)−1-PE and (+)−1-PE in aqueous solution. The error bars on the *y* axis represent the standard deviation of the removal efficiency measured in the kinetic adsorption experiments ($n = 3$, see details in "Methods"). **f** Efficient sieving of constitutional and stereo isomers by anisotropic HOG membrane.

ethylene oxide and water molecules[36,37]. As a result, the aromatic helix with a wide distribution transforms into a narrow structure with a flat interface through dynamic hydrogen bonding to reduce the interfacial energy associated with unfavorable segmental contacts (Supplementary Fig. 6b, c)[38]. To provide further evidence of dynamic hydrogen bonding between aromatic segments in the formation of aligned gels, the helical polymer **2*S*** was prepared with the aim of frustration of dynamic interaction within aromatic skeleton (Fig. 3f). As expected, **2*S*** showed apparent cotton effect in the range of aromatic segments, indicative of the formation of helical aggregates (Supplementary Fig. 5e). In great contrast, the helix of **2*S*** entangled each other to result in amorphous gel (**ROG2*S***) (Supplementary Fig. 5d, f).

Membrane separation with regioselectivity and enantioselectivity

Owing to the high degree of insertion of aromatic channels in the gel matrix, **HOG1*S*** was used as a highly selective molecular transport membrane. The impact was studied by the filtration of various phenethyl alcohol (PE) solutes with constitutional and stereo-isomeric structures in aqueous solution by the use of dialysis membrane (DM, MW 500 Da) with the loading of poly ethylene glycol gel (PEG, MW 1000 Da), **ROG2*S*** and **HOG1*S*** (Fig. 4a). Compared to pure gel (PEG), the **ROG2*S*** and **HOG1*S*** membranes with hetero porours structures gave considerable rejection rate and permselectivity. As shown in Fig. 4a, the fluxes of1-PE (0.02 wt%) and 2-PE (0.02 wt%) through the **PEG** membrane were 27.22 μg cm^{-2} h^{-1} and 27.30 μg cm^{-2} h^{-1}, respectively. However, the permeation rates of 2-PE (0.02 wt%) obviously decreased to 21.88 μg cm^{-2} h^{-1} and 19.35 μg cm^{-2} h^{-1} by the use of **ROG2*S*** and **HOG1*S*** membranes, while the rates of 1-PE (0.02 wt%) dramatically reduced to 21.71 μg cm^{-2} h^{-1} and 17.43 μg cm^{-2} h^{-1}, respectively, indicating strong adsorption between the membrane and aromatic feeds. On the basis of their permeance rates, the permselectivities of constitutional isomers were calculated as 1.01 for the **ROG2*S*** membrane and 1.11 for the **HOG1*S*** membrane. Therefore, the selective separation of hetero-pore membranes was further operated by the retarded transport mechanism driven by gel loading[39]. With the increasing quantity of gels, the fluxes of both 1-PE and 2-PE gradually decreased due to the significant increase in the mass transfer distance (Fig. 4b). Regardless of the loading of both gels, the permeation rate of 2-PE was always greater than that of 1-PE, demonstrating that the permeation selectivity is based on the binding affinity of the substance with the membranes. It is notable that the selectivity was stabilized at 1.02 as the loading of **ROG2*S*** increased to 150 μL, whereas **HOG1*S*** with the same loading gave rise to greater permselectivity up to 1.92, indicating that the remarkable selection of **HOG1*S*** is attributable to the continuous sieving effect of the high organization of aromatic fillers[8,40]. To clearly demonstrate the separation advantages of the **HOG1*S*** membrane, the permeation of an isomeric mixture (1:1) with different gels was tested (Supplementary Fig. 8b). As expected, **HOG1*S*** exhibited excellent regioselectivity by only allowing 2-PE molecules to pass through the membrane while almost retaining 1-PE molecules, resulting in an ultra-high separation factor of 11.46. These results indicated that the addition of aromatic filler optimizes the selectivity of hydrogel membranes.

Notably, we found that the **HOG1*S*** membrane has a favorable enantioseparation efficiency for racemic solutions of (±)−1-PE. Variation in the fluxes and enantiomeric excess of the racemates with gel loading was observed (Fig. 4c). Under the optimal conditions, the enantioselectivity reached 92% ee for (-)−1-PE when 175 μL of **HOG1*S*** (22 mM) was loaded. On the other hand, the isomeric gel of **HOG1*R*** showed excellent selectivity for (+)−1-PE up to 90% ee, resulting in the selective and rapid transport of (+)-enantiomeric feed (Supplementary

Fig. 8e). The comprehensive performance of **HOG1*S*** motivated us to explore the efficient sieving behavior among constitutional isomers and stereoisomers. Separation was performed with the permeation of an equal amount of mixed PE solution (0.01 wt%) by loading 175 μL of **HOG1*S*** (22 mM) (Fig. 4d). To corroborate the selection, the filtrate was monitored every hour by high-performance liquid chromatography (HPLC). Consistent with the order of permeation flux determined from single-component filtration, 2-PE breaks through the membrane first, followed by (−)−1-PE and finally (+)−1-PE. Dynamic regio- and enantioselectivity were calculated according to the breakthrough curves. As shown in Supplementary Fig. 8f, the separation factor of the constitutional isomers was 11.3, whereas the enantioselectivity for (+)−1-PE was 87% ee. Overall, no noticeable decrease was observed in the selection of constitutional isomers and stereoisomers during the separation of the three-component mixture, revealing that shape-persistent **HOG1*S*** is well suited for cascade separation (Fig. 4f).

Sieving ability from binding selection

The sieving of highly ordered gel membranes most likely occurs with the selective adsorption of aromatic fillers. To provide evidence, we further compared the uptake of phenethyl alcohol isomers. Eventually, the **HOG1*S*** suspension (5.5 mM) removed most of the solute from the 0.002 wt% aqueous solution. The equilibrium uptake of all phenethyl alcohol was calculated as 125–130 mg g^{-1} owing to the similar kinetic diameters of the isomeric structures. Nonetheless, a sharp difference was observed in kinetic adsorption (Fig. 4e). The **HOG1*S*** suspension removed (+)−1-PE much more quickly than all other isomers, reaching ~50% of its equilibrium uptake was needed 25 min. Meanwhile, 42% of (−)−1-PE and 37% of 2-PE were removed. Likewise, it took 90 min for removing 2-PE to reach its equilibrium, but removing (−)-1-PE and (+)-1-PE required 60 min and 45 min, respectively. Moreover, the adsorption better fit pseudo-second-order (PSO) kinetics (Supplementary Fig. 10) because of the chemical adsorption between aromatic pores and the phenylene segment. The rate constant (K_{obs}) of (+)-1-PE was fitted to 0.15 mg g^{-1} min^{-1}, which is 1.5 times greater than the constant of (−)-1-PE and two times greater in magnitude than the constant of 2-PE, indicating that the selectivity is based on adsorption ability (Supplementary Fig. 10d).

To gain insight into adsorption selectivity, the binding energies between the aromatic filler and phenethyl alcohol isomers were compared by molecular dynamics calculations (Supplementary Fig. 11). In contrast to 1-PE enantiomers, 2-PE easily forms intramolecular H-bonds through O−H···π interaction, hindering the intermolecular interactions between 2-PE and aromatic channels[41]. When the phenyl group of 1-PE with a (+)-conformation approached **HOG1*S***, both the methylene and hydroxyl groups were far from the aromatic fillers. However, these large groups of the (-)-enantiomer were close to the aromatic fillers, resulting in a large space crowding within the chiral interfaces, which was reflected in the low negative binding energies. The computational results reveal the selective sieving by **HOG1*S*** in terms of high regioselectivity and enantioselectivity, which are consistent with the experimentally observed trend.

Discussion

In conclusion, a bottom-up strategy for the construction of oriented MMMs has been presented via the orthogonal assembly of heteroporous precursors through dynamic hydrogen bonding. Simultaneous thermodynamic processes in the immiscible segments spontaneously induced straight adsorbing channels in the polymer matrix, enabling the preferential transport of 2-phenylethanol among phenethyl alcohol mixtures with a remarkable separation factor up to 11.46. Supramolecular chirality was also introduced into the specific adsorbent through a self-repairing process, which leads to excellent enantioselectivity for racemic 1-phenylethanol with 92% ee. This is great contrast to reported MMMs, which rely on a series of noncovalent interaction between the adsorptive filler and the polymer matrix, giving improved long-term stability and reusability[42–46]. We believe that our strategy will contribute to energy conservation as well as to specific adsorptive separation.

Methods

General

The purity of the products was checked by thin-layer chromatography (TLC; Merck, silica gel 60). High-performance liquid chromatography (HPLC) was performed for further purification by using Hanban Sci&Tech NP7000 SERIALS PUMP, NU3000 SERIALS UV/VIS DETECOR, C18 column (Hedera ODS−2 column). ^{1}H-NMR and ^{13}C-NMR spectra were recorded from $CDCl_3$ or d_4-MeOH solutions on Bruker AVANCE III 400 MHz. All compounds are subjected to ^{1}H NMR analysis to confirm ≥98% sample purity with the residual solvent peak. MALDI TOF-MS spectroscopy (MALDI-TOF-MS) was performed on Bruker ESI-Q-TOF maXis 4 G using α-cyano-4-hydroxy cinnamic acid (CHCA) as a matrix. Vapor pressure osmometry (VPO) experiments were recorded on the OSMOMAT 070 instrument, and both measurements were used polyethylene glycol (average molecular weight = 4000 g mol^{-1}) as a standard for the determination of the value of K. X-ray photoelectron spectroscopy (XPS) measurements were performed on ESCALab250 Mark (VG) photoelectron spectrometer using a monochromatic Al K_α X-ray source. X-ray scattering measurements were performed by Xeuss 3.0 HR. UV/Vis spectra measurements were obtained from the Metash UV-8000S Spectrophotometer. Fluorescence spectra measurements were obtained from a Hitachi F-4500 Fluorescence Spectrophotometer. Circular Dichroism (CD) Spectra measurements were obtained from a JASCO J-81003040414 spectropolarimeter. Transmission electron microscopy (TEM) measurements were performed at 80 kV using a JEM ARM 200 machine. AFM measurements were performed using Bruker Multimode 8 in air at ambient temperature (ca. 25 °C) on mica with tapping mode. Rheology experiments were performed by ARES/RFS II from TA Instrument.

AFM experiments

For the AFM measurement of the assembled structures, the buffer solution (Na_2HPO_4/NaOH) of **1*S*** or **1*R*** (11–110 μM) was prepared, and 10 μL of the samples was cast on mica. After slow evaporation under air at room temperature, the AFM was performed with tapping mode. The typical settings of the AFM for the high-magnification observations were as follows: a free amplitude of the oscillation frequency of 1.0–1.5 V, a set-point amplitude of 0.9–1.4 V, and a scan rate of 1.0 Hz.

TEM experiments

To investigate the assembly of **1*S*** in buffer solution (11–110 μM, Na_2HPO_4/NaOH), a drop of the above stock solution was placed on a carbon-coated copper grid, and the solution was evaporated under ambient conditions. The dried specimen was observed using the JEM −2010HR machine operated at 200 kV.

XPS experiments

To confirm the state of phenol of **1*S*** in the buffer solution of Na_2HPO_4/NaOH. The solution of **1*S*** (11 μM) was freeze-dried for XPS testing.

Computation

An initial model of right-handed tubes was constructed according to the calculation from the XRD result of **1*S***, so that the potential energy was minimized. The porous tubules with right-handedness were constructed from sixteen molecules to form a single helix. To gain a deeper understanding of the isomeric separation mechanism, 1:1 binding energies of host–guest interactions between **1*S*** and phenethyl alcohol isomers on the side of the helical tubular wall were calculated using the Material Studio 8.0 program. The calculations were performed by Forcite Tools based on molecular mechanics theory and

molecular dynamics theory under the following parameters: task: energy; quality: ultrafine; forcefield: compass; charge: forcefield assigned; electrostatic: atom based; van der Waals: atom based; job description: 5000; run in parallel on: 1 of 8 cores. The binding energy was calculated employing the following equation:

$$E_B = E_{total} - E_{\boldsymbol{HOG1S}} - E_{PE} \quad (1)$$

Herein, E_B delineates the binding energy, E_{total} signifies the total energy of the whole system, and $E_{\boldsymbol{HOG1S}}$ along with E_{PE} denote the total energies of **HOG1*S*** and phenylethanol isomers.

The membrane separation in the selective filtration of PE solutes

To investigate the retarded transport, dialysis membrane (MW 500 Da) with and without of gel loading such as polyethylene glycol (Mn 1000, 4 wt%, 50 μL), **ROG2*S*** (4 wt%, 50 μL) and **HOG1*S*** (22 mM, 50 μL) were used as separation membranes for compaision. After carefully filling the corresponding volume of the gel into the dialysis membrane and removing air bubbles, they were secured to the ultrafiltration centrifuge tubes. After building up the platform, the filtration of the isomeric feeds of phenethyl alcohol solution was performed in the same procedure. For example, the feeds of 1-PE and 2-PE with the variation of concentration in aqueous solution (0.02-0.04 wt%) were added to centrifuge tubes. After centrifuge with the rotated speed of 7500 rpm, the fluxes were monitored hourly by HPLC (chiralcel AD-H column, mobile phase: hexane/i-PrOH = 98/2, flow rate: 1 mL min^{-1}, detection wavelength: 210 nm). In order to investigate the effect of membrane thickness, the filtration of 2-PE and 1-PE aqueous solution (0.02 wt%) with the variation of gel loading (25–150 μL) was also performed. Meanwhile, the separation factor of constitutional isomers was further observed by the filtration of equal mixtures of 2-PE and 1-PE solution (0.02 wt%) by the use of gels, including PEG (150 μL, 4 wt%), **ROG2*S*** (150 μL, 4 wt%), and **HOG1*S*** (150 μL, 22 mM) based on the permeance rates. In addition, the permselectivity of 1-PE enantiomers was observed by the filtration of (+)-1-PE and (-)-1-PE with the variation of concentration in aqueous solution (0.01–0.03 wt%), while the effect of gel loading (25-175 μL) was observed by the filtration of (+)-1-PE and (-)-1-PE aqueous solution (0.01 wt%). Furthermore, the enantiomeric excess by kinetic resolution of racemic mixture (±)-1-PE (0.01 wt%) was investigated by the use of **HOG1*S*** (25-175 μL, 22 mM). To investigate the comprehensive performance of a highly ordered anisotropic gel, the cascade separation for an equally mixed solution of 2-PE, (-)-1-PE, and (+)-1-PE (0.01 wt%) was explored under 175 μL of **HOG1*S*** (22 mM). The total number of independent measurements of each membrane separation test conducted in this work is three times, respectively. The permeation flux (J), permselectivity (S), and separation factor (α) were calculated via the following equations:

$$J = \frac{Q}{A \times t} \quad (2)$$

where Q (μg) is the mass of penetrated solute, A (cm^2) is the effective area of the membrane, and t (h) is the centrifugal time.

The permselectivity (S) is defined as the ratio of the permeance of 2-PE over 1-PE or (-)-1-PE over (+)-1-PE in single feed solution, via the following equation:

$$S = \frac{J_1}{J_2} \quad (3)$$

where J_1 (μg cm^{-2} h^{-1}) is the permeation fluxes of 2-PE or (-)-1-PE, J_2 (μg cm^{-2} h^{-1}) is the permeation fluxes of 1-PE or (+)-1-PE.

The separation factor (α) is often used as a parameter to assess separation performance and is the ratio of the permeate composition over the mixed feed solution, via the following equation:

$$\alpha = \frac{Y_1/Y_2}{X_1/X_2} \quad (4)$$

where Y_1 and X_1 are the percentages of 2-PE in the permeate and feed, respectively, and Y_2 and X_2 are the percentages of 1-PE in the permeate and feed, respectively.

Kinetic adsorption experiments

All kinetic adsorption experiments were performed using the same procedure. A representative example is described for the adsorption of **HOG1*S*** for 2-phenethyl alcohol at room temperature. To assess the maximum removal efficiency for 2-phenethyl alcohol, the adsorption kinetic experiments were conducted with time variation. Firstly, the semi-permeable membrane with stock gel of **HOG1*S*** (100 μL, 5.5 mM) was added to 10 mL of 2-phenethyl alcohol solution (0.002 wt%). Then the mixture was shaken at room temperature. In total, 0.2 mL of the solution was taken out via a syringe with time variation from 0 to 180 min. The total number of independent measurements of each membrane separation test conducted in this work is three times, respectively. The series of equilibrium concentrations was monitored by UV/Vis spectroscopy to obtain the adsorption kinetic curves.

The efficiency of 2-phenethyl alcohol removal (%) by the **HOG1*S*** was determined by the following equation:

$$Removal\ efficiency = \frac{C_0 - C_t}{C_0} \quad (5)$$

where C_O (mg L^{-1}) and C_t (mg L^{-1}) are the initial and real-time concentration of 2-phenethyl alcohol in filtrates, respectively.

Data availability

All data in the main text or the Supplementary Information is available from the corresponding author upon request. Source data are provided with this paper.

References

1. Pacchioni, G. A chiral supramolecular MOF for enantiomer separation. *Nat. Rev. Mater.* **8**, 363 (2023).
2. Chen, C. et al. Hydrogen-bonded organic frameworks for membrane separation. *Chem. Soc. Rev.* **53**, 2738–2760 (2024).
3. Drew, D., North, R., Nagarathinam, K. & Tanabe, M. Structures and general transport mechanisms by the major facilitator superfamily (MFS). *Chem. Rev.* **121**, 5289–5335 (2021).
4. Drew, D. & Boudker, O. Shared molecular mechanisms of membrane transporters. *Annu. Rev. Biochem.* **85**, 543–572 (2016).
5. Oh, H. et al. Approaching ideal selectivity with bioinspired and biomimetic membranes. *ACS Nano* **19**, 31–53 (2025).
6. Shen, Y., Saboe, P., Sines, I., Erbakan, M. & Kumar, M. Biomimetic membranes: a review. *J. Membr. Sci.* **454**, 359–381 (2014).
7. Dechnik, J., Gascon, J., Doonan, C., Janiak, C. & Sumby, C. Mixed–matrix membranes. *Angew. Chem. Int. Ed.* **56**, 9292–9310 (2017).
8. Datta, S. et al. Rational design of mixed–matrix metal–organic-framework membranes for molecular separations. *Science* **376**, 1080–1087 (2022).
9. Niu, Z. et al. Mixed matrix membranes for gas separations: a review. *Chem. Eng. J.* **494**, 152912 (2024).
10. Cheng, Y. et al. Advances in metal–organic framework-based membranes. *Chem. Soc. Rev.* **51**, 8300–8350 (2022).
11. Jin, Y., Li, M. & Yang, Y. Covalent organic frameworks for membrane separation. *Adv. Sci.* **12**, 2412600 (2025).
12. Guo, Z. et al. Reverse filling approach to mixed matrix covalent organic framework membranes for gas separation. *Nat. Commun.* **16**, 3617 (2025).

13. Jia, L., Tang, X., Cui, Y. & Liu, Y. Porous metal–organic cage-based membranes. *Sci. China Chem.* **66**, 2169–2180 (2023).
14. Zhang, J. et al. Support-layer integrated zeolite membranes through in situ interfacial transformation of clay-based proto-membranes. *Angew. Chem. Int. Ed.* **64**, e202420696 (2025).
15. Chen, G. et al. Solid-solvent processing of ultrathin, highly loaded mixed-matrix membrane for gas separation. *Science* **381**, 1350–1356 (2023).
16. Liu, G. et al. Mixed matrix formulations with MOF molecular sieving for key energy-intensive separations. *Nat. Mater.* **17**, 283–289 (2018).
17. Li, C. et al. Establishing gas transport highways in MOF-based mixed matrix membranes. *Sci. Adv.* **9**, eadf5087 (2023).
18. Liu, J., Zou, G. & Hou, S. Chiral gold nanoparticles/graphene oxide membranes with ultrahigh and stable permeance for sieving and enantioseparation. *Chem. Eng. J.* **467**, 143366 (2023).
19. Sun, H. et al. Aromatic–aliphatic hydrocarbon separation with oriented monolayer polyhedral membrane. *Science* **386**, 1037–1042 (2024).
20. Wei, P., Yan, X. & Huang, F. Supramolecular polymers constructed by orthogonal self-assembly based on host-guest and metal-ligand interactions. *Chem. Soc. Rev.* **44**, 815–832 (2014).
21. Zeng, H. et al. Orthogonal-array dynamic molecular sieving of propylene/propane mixtures. *Nature* **595**, 542–548 (2021).
22. Fan, H. et al. MOF-in-COF molecular sieving membrane for selective hydrogen separation. *Nat. Commun.* **12**, 38 (2021).
23. Liu, R. et al. Evolution of protein assemblies driven by the switching of interplay mode. *ACS Nano* **17**, 2245–2256 (2023).
24. Qian, C. et al. Toward covalent organic frameworks bearing three different kinds of pores: the strategy for construction and COF-to-COF transformation via heterogeneous linker exchange. *J. Am. Chem. Soc.* **139**, 6736–6743 (2017).
25. Feng, X., Ding, X. & Jiang, D. Covalent organic frameworks. *Chem. Soc. Rev.* **41**, 6010–6022 (2012).
26. Mou, Q. et al. Topology of gemini-shaped hexagonal heterojunction for efficient stereoconvergent transformation via dynamic kinetic resolution. *Angew. Chem. Int. Ed.* **64**, e202417870 (2025).
27. Li, Y. et al. Precisely controlled multidimensional covalent frameworks: polymerization of supramolecular colloids. *Angew. Chem. Int. Ed.* **59**, 21525–21529 (2020).
28. Lin, R. & Chen, B. Hydrogen-bonded organic frameworks: chemistry and functions. *Chem* **8**, 2114–2135 (2022).
29. Reddy, P. G. & Domb, A. J. Bioactive phenolate salts: thymol salts. *ChemMedChem* **18**, e202300045 (2023).
30. Beamson, G., Briggs, D. *High Resolution XPS of Organic Polymers –The Scienta ESCA 300 Data Base* (John Wiley & Sons, 1992).
31. Tian, Z. et al. Synthesis of biologically derived poly(pyrogallol) nanofibers for antibacterial applications. *J. Mater. Chem. B* **11**, 3356–3363 (2023).
32. Cho, Y. et al. A double–walled hexagonal supermolecule assembled by guest binding. *J. Am. Chem. Soc.* **123**, 1258–1259 (2001).
33. Hashim, P. K., Bergueiro, J., Meijer, E. W. & Aida, T. Supramolecular polymerization: a conceptual expansion for innovative materials. *Prog. Polym. Sci.* **105**, 101250 (2020).
34. Nancy, A. C. & Suthanthiraraj, S. A. Effect of Al_2O_3 nanofiller on the electrical, thermal and structural properties of PEO:PPG based nanocomposite polymer electrolyte. *Ionics* **23**, 1439–1449 (2017).
35. Kim, H., Zin, W. & Lee, M. Anion–directed self-assembly of coordination polymer into tunable secondary structure. *J. Am. Chem. Soc.* **126**, 7009–7014 (2004).
36. Huang, Z. et al. Responsive nematic gels from the self-assembly of aqueous nanofibres. *Nat. Commun.* **2**, 459 (2011).
37. Li, J. T. & Chen, B. L. Flexible hydrogen–bonded organic frameworks (HOFs): opportunities and challenges. *Chem. Sci.* **15**, 9874–9892 (2024).
38. Wang, W. et al. Orthorhombic covalent organic frameworks with fmj topology as photocatalyst for hydrogen evolution. *Angew. Chem. Int. Ed.* **64**, e202418086 (2025).
39. Jönsson, A., Gürbüz, H., Wildfang, L., Jensen, P. R. & Dufva, M. Tissue like density sheets of hepatoblastoma cultures obtained with thin suspended hydrogels mimicking in vivo inter-capillary distances. *Adv. Mater. Technol.* **10**, 2401204 (2025).
40. Zhao, C. et al. Polyamide membranes with nanoscale ordered structures for fast permeation and highly selective ion-ion separation. *Nat. Commun.* **14**, 1112 (2023).
41. Varfolomeevaa, V., Terent'eva, A. & Buryak, A. K. The influence of intramolecular hydrogen bonds on the adsorption properties of aromatic alcohols and thiols. *Russ. J. Phys. Chem.* **82**, 906–910 (2008).
42. Lu, Y. et al. Homochiral MOF-polymer mixed matrix membranes for efficient separation of chiral molecules. *Angew. Chem. Int. Ed.* **58**, 16928 (2019).
43. Cheng, S. Q. et al. Chiral macrocyclic membranes for efficient enantioselective separation. *Sci. China Chem.* **69**, 1259–1265 (2026).
44. Li, R. H. et al. Discrete chiral metallacycle-based membrane for highly efficient enantioseparation. *Adv. Funct. Mater.* **35**, 2502767 (2025).
45. Chan, J. Y. et al. Incorporation of homochirality into a zeolitic imidazolate framework membrane for efficient chiral separation. *Angew. Chem. Int. Ed.* **57**, 17130 (2018).
46. Huang, G., Wang, Y., Du, Y., Long, Q. & Chai, K. Unraveling the efficient separation of positional phenylethanol isomers by aluminum-based metal-organic frameworks: the role of pore geometry and multiple molecular interactions. *Appl. Surf. Sci.* **714**, 164385 (2025).

Author contributions

Q.M. performed most of the experiments and analyzed the data. C.P.C. and X.L. performed VPO and separation experiments. Y.X.S. performed AFM experiments. T.Y.Z. performed TEM experiments. J.H.W. and Y.R.L. performed XRD experiments. H.L.T. and L.Y.J. performed GPC experiments. M.L. and Y.Z. gave greater guidance. Z.H. designed the whole work.

Funding

This work was supported by the Crossing Research Funds for the Central University (HT-99982024-0117, HT-99982025-0152).

Competing interests

The authors declare no competing interests.

Additional information

Supplementary information The online version contains supplementary material available at https://doi.org/10.1038/s41467-026-75619-z.

Correspondence and requests for materials should be addressed to Yongri Liang, Zhegang Huang or Myongsoo Lee.

Peer review information *Nature Communications* thanks Jian Jin and the other, anonymous, reviewer(s) for their contribution to the peer review of this work. A peer review file is available.